Layer dependent topological phases and transitions in $TaRhTe_4$: From monolayer and bilayer to bulk

Xiao Zhang [1,2,*] Ning Mao,[3] Oleg Janson [1] Jeroen van den Brink [1,2,4] and Rajyavardhan Ray [1,4,5,†]

[1]*Institute for Theoretical Solid State Physics, Leibniz Institute for Solid State and Materials Research Dresden, Helmholtzstr. 20, D-01069 Dresden, Germany*

[2]*Institute of Theoretical Physics and Würzburg-Dresden Cluster of Excellence ct.qmat, Technische Universität Dresden, 01062 Dresden, Germany*

[3]*Max Planck Institute for Chemical Physics of Solids, D-01187 Dresden, Germany*

[4]*Dresden Center for Computational Materials Science (DCMS), TU Dresden, 01062 Dresden, Germany*

[5]*Department of Physics, Birla Institute of Technology Mesra, Ranchi, Jharkhand 835215, India*

(Received 18 March 2024; revised 15 July 2024; accepted 8 August 2024; published 3 September 2024)

The recently synthesized ternary quasi-2D material $TaRhTe_4$ is a bulk Weyl semimetal with an intrinsically layered structure, which poses the question of how the topology of its electronic structure depends on layer separations. Experimentally, these separations may be changed for instance by intercalation of the bulk, or by exfoliation, to reach monolayer or few-layer structures. Here, we show that in the monolayer limit a quantum spin Hall insulator (QSHI) state emerges, employing density functional calculations as well as a minimal four-orbital tight-binding model that we develop. Even for weak spin-orbit couplings the QSHI is present, which has an interesting edge state that features Rashba-split bands with quadratic band minima. Further, we find that a weak topological insulator (WTI) manifests in the bilayer system due to sizable intralayer hopping, contrary to the common lore that only weak interlayer interactions between stacked QSHIs lead to WTIs. Stacked bilayers give rise to a phase diagram as a function of the interlayer separation that comprises a Weyl semimetal, WTI, and normal insulator (NI) phases. These insights on the evolution of topology with dimensions can be transferred to the family of layered ternary transition metal tellurides.

DOI: 10.1103/PhysRevMaterials.8.094201

I. INTRODUCTION

Topological insulators (TIs) and topological semimetals are new classes of quantum materials [1–6] with potential applications in spintronics and quantum computation [7–9]. TIs feature a nontrivial bulk insulating gap accompanied by topologically robust gapless edges for two-dimensional (2D) TIs or surface states in three-dimensional (3D) TIs with linearly dispersing double degenerate bands meeting at Dirac points [10–13]. 2D TIs are characterized by a $\mathcal{Z}_2$ topological index and are also known as quantum spin Hall insulators (QSHI) [14–17]. For 3D TIs, however, four indices $\mathcal{Z}_2 = (\nu_0; \nu_1\nu_2\nu_3)$ are required based on which they can be classified as strong ($\nu_0 = 1$) or weak ($\nu_0 = 0$; $\nu_i = 1$ for any i) [18,19]. Correspondingly, strong (weak) TIs possess surface states with an odd (even) number of Dirac bands on all (selected) facets [20–22]. Arguably, the simplest weak TI (WTI) is obtained by stacking of QSHIs whereby the facets perpendicular to the stacking direction are free of Dirac nodes [11,23].

Weyl semimetals (WSMs), on the other hand, host pairs of topologically protected linear band crossings, called Weyl points (WPs) [4,5,24]. Each WP is characterized by a topological charge and chirality $\chi = \pm 1$ [25–27]. The surface states of WSMs are Fermi arcs that terminate at the projections of bulk WPs of opposite chirality [28–30].

In recent years, a large number of TIs and WSMs have been experimentally realized, for example, monolayer $1T'$-WTe_2 as QSHI [17,31]; Bi_2Se_3 [32,33] and Bi_2Te_3 [34,35] as 3D strong TIs; $Bi_{14}Rh_3I_9$ [36] and $Bi_{12}Rh_3Cu_2I_5$ [37] as WTIs; TaAs, [38,39] WTe_2 [40,41], $MoTe_2$ [42,43] and $TaIrTe_4$ [44,45] as WSMs. Many such compounds are layered materials with van der Waals (vdW) type interlayer interactions, and exhibit different properties as a function of layer thickness [46–50]. Of particular relevance are binary and ternary tellurides known to be WSMs in the bulk while the monolayers are QSHIs. From the practical angle, QSHIs with large bulk topological gaps for room temperature applications and/or WSMs with minimal symmetry-allowed WPs near the Fermi energy are desired. At the same time, lack of a clear understanding of the topological phase transitions as a function of the number of layers is detrimental to possible application in the development of efficient quantum devices.

Here, we focus on the recently synthesized layered ternary quasi-2D material $TaRhTe_4$ [51–53] and elucidate the topological electronic properties of different layered structures, from monolayer and bilayer to bulk, using density functional theory (DFT). $TaRhTe_4$ is isostructural to $TaIrTe_4$ [44,45,54] and both share the same nonsymmorphic space group as 3D WTe_2 [24,40,55], all of which are type-II WSMs in bulk. In comparison, the monolayers of $TaIrTe_4$ and $1T'$-WTe_2 are QSHIs with time-reversal protected edge states [31,56–58].

*Contact author: x.zhang@ifw-dresden.de
†Contact author: r.ray@bitmesra.ac.in

Interestingly, the bilayer $TaIrTe_4$, owing to its relatively small interlayer separation, has been predicted to be a QSHI as well [50]. With increasing interlayer separation, there is a phase transition to a normal insulator phase. Although remarkable, the QSHI ground state in the bilayer $TaIrTe_4$ is at odds with the common understanding that interlayer coupling between stacked QSHIs gaps out the edge states, leading to a trivial phase [25]. Furthermore, it is unknown which topological phase transitions (TPTs) occur while increasing the layer thickness from the monolayers and bilayers to the bulk in any layered chalcogenide, which can be important to bring to fruition the envisioned technological applications of these materials.

In this work, we establish that the ambient structures of monolayer as well as bilayer $TaRhTe_4$ are QSHIs. The monolayer has a bulk gap of $\sim$65 meV, indicative of insulating behavior at room temperature, while the bilayer is a zero gap semimetal with an average direct topological gap of $\sim$50 meV around Γ. We obtain a minimal four-orbital tight binding (TB) model for the monolayer which reveals that the QSHI phase is driven by hybridization between Ta-$5d_{x^2-y^2}$ and Te-$5p_x$ orbitals. Our analysis of the interlayer and intralayer hoppings for the bilayer QSHI elucidates the importance of interlayer hoppings in the stabilization of the QSHI phase, suggesting that the bilayer $TaRhTe_4$ behaves effectively as a single electronic entity despite vdW-separated physical layers in the unit cell.

Finally, the bulk $TaRhTe_4$ is confirmed to be a WSM with three quartet WPs close to Fermi energy arising from band crossings between the top of the valence band and the bottom of the conduction band (bands N and $N+1$ where N is the number of valence electrons). Topological phase transitions between WSM, WTI, and NI phase are realized by calibrating the intra- and interbilayer distances, culminating in a rich phase diagram. The topological phase transition of WTI-NI is the same as that in the bilayer $TaRhTe_4$. Phase transitions of WSM-WTI and WSM-NI open up a band gap near the Fermi level and are accompanied by the creation and annihilation of WPs. Interestingly, we observe that the WPs remain confined in the $k_z = 0$ plane for WSM-NI as well as WSM-WTI transitions.

II. MONOLAYER SYSTEM

A. Crystal structure and symmetries

The three-dimensional $TaRhTe_4$ crystallizes in the noncentrosymmetric $Pmn2_1$ (31) space group, shown in Fig. 1(a), similar to WTe_2 and $TaIrTe_4$. Each unit cell consists of two AB-stacked $TaRhTe_4$ formula units and possesses mirror M_x, glide mirror $\widetilde{M}_y = t[(\mathbf{R}_x + \mathbf{R}_z)/2]M_y$, and two-fold screw $\widetilde{C}_{2z} = t(\mathbf{R}_z/2)C_{2z}$ symmetries. Here, $t(\mathbf{R}_\mu)$ represents translations by a lattice constant along $\mathbf{e}_\mu$, M_x represents a mirror plane with normal along $\mathbf{e}_x$ direction, while C_{2z} represents twofold rotational symmetry about the $\mathbf{e}_z$ axis.

The 2D monolayer $TaRhTe_4$ was constructed out of the bulk crystal structure by inserting large vacuum ($\gtrsim$20 Å) between the AB-stacked layers of the bulk unit cell (see Methods for details). Figure 1(b) shows the top view of monolayer $TaRhTe_4$, Ta and Rh atoms forming zigzag chains along the

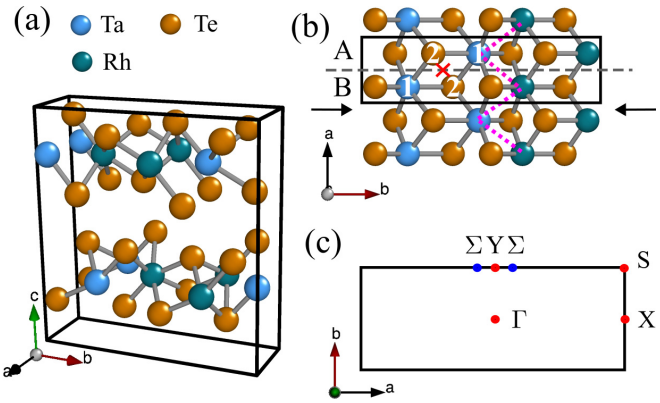

FIG. 1. (a) Crystal structure of bulk and (b) monolayer $TaRhTe_4$ (top view) where the unit cell is shown in solid black lines. In the latter, the sublattices A and B are also shown. The orbitals of Ta(Te)-atoms marked by 1A and 1B (2A and 2B) mainly contribute to a minimal tight-binding model. The effective inversion center, marked by a cross, lies at the center of this Ta-Te plaquette. (c) Brillouin zone (BZ) of monolayer $TaRhTe_4$ along with the high-symmetry points.

a axis. The resulting structure is dynamically stable [see Supplemental Material (SM) [59] for the phonon dispersion]. In comparison to bulk, an effective inversion symmetry can be found in the monolayer $TaRhTe_4$. Apart from the time-reversal symmetry $\mathcal{T}$ and lattice translations $\{t(\mathbf{R}_x), t(\mathbf{R}_y)\}$, the monolayer structure also has a glide reflection $\widetilde{M}_x = t(\mathbf{R}_y/2)M_x$ and a two-fold screw rotation $\widetilde{C}_{2x} = t(\mathbf{R}_x/2)C_{2x}$. The product of these two generators is exactly the spatial inversion symmetry $\widetilde{M}_x\widetilde{C}_{2x} = \mathcal{I}$ [31,45,58,60]. The corresponding inversion center lies at the center of the line joining the Ta atoms. Consequently, the monolayer unit cell can be thought of as composed of sublattices A and B. The atoms in different sublattices are related to each other via the effective inversion symmetry, as shown in Fig. 1(b). The corresponding BZ along with the high-symmetry points are shown in Fig. 1(c).

B. Electronic properties

In Fig. 2(a), the band structure, obtained within scalar relativistic approximation ('no SOC'), of monolayer $TaRhTe_4$ along a high-symmetry path in BZ is shown. It is a Dirac semimetal with two Dirac nodes located at $\Sigma = (\pm 0.0833, 0.253)\,\text{Å}^{-1}$ along the Y-S path, as expected for a nonsymmorphic crystal structure [31]. By analyzing the density of states (not shown), we found that Ta-$5d$ and Te-$5p$ orbitals dominate around the Fermi level, whereas the contribution of Rh-$4d$ orbitals is negligible. We thus show the band-weight contributions from Te-$5p_x$ and Ta-$5d_{x^2-y^2}$ orbitals in Fig. 2(a). The overlap of orange and blue dots implies a p-d hybridization around the Dirac cone, which is analogous to the case in monolayer $TaIrTe_4$ [50]. It is important to note that band inversion is present, similar to the case of $1T'$-WTe_2 [31,58,60].

As shown in Fig. 2(b), SOC lifts the degeneracy of the Dirac point and opens up a gap $E_g \sim 65$ meV, which is sufficiently large for room-temperature QSHI applications. Due to the effective inversion symmetry and time-reversal symmetry,

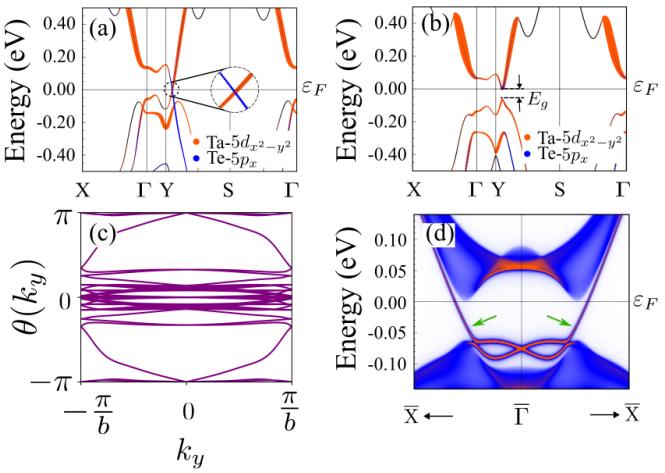

FIG. 2. Electronic properties of monolayer $TaRhTe_4$. Band structure and orbital contributions close to the Fermi energy ε_F in monolayer $TaRhTe_4$ (a) without ('no SOC') and (b) with SOC. The inset provides a zoomed view of the Dirac cone. (c) Wilson loop spectrum for the full DFT band structure when the BZ loop is chosen along k_x direction. (d) Surface spectral function for the termination shown in Fig. 1(b). The edge states are marked by green arrows.

each band is doubly degenerate. Further, the Wilson loops [61] in Fig. 2(c) indicate that the bands are topologically nontrivial, with the topological invariant $\mathcal{Z}_2 = 1$.

Figure 2(d) displays an edge state spectrum of monolayer $TaRhTe_4$ in a nanoribbon geometry for the edge terminations marked by arrows in Fig. 1(b). Indeed, a pair of counter-propagating edge states cross at $\bar{\Gamma}$ and carry opposite spin polarization. It is interesting to note that the topological edge Dirac cone lies within the bulk gap and resembles Rashba splitting of edge states with parabolic band minima akin to the nearly free electron dispersion. However, the energy position of the Dirac point is sensitive to the nanoribbon/edge termination (see SM [59] for details).

C. Four-band minimal tight-binding model

To further understand the electronic properties of monolayer $TaRhTe_4$, especially the role of SOC, we obtain a minimal TB model. A minimal TB model is also helpful in investigations of transport properties and studies of disorder effects, among others [57,62]. As shown in the inset of Fig. 2(a), the orbital contributions to states close to the Fermi energy are predominantly from Ta-5$d_{x^2-y^2}$ orbitals and 5p_x orbitals centered at one of the Te atoms marked by atoms 1 and 2 in Fig. 1(b) and their sublattice symmetry partners (A/B). We, therefore, construct a maximally projected Wannier model using a four-orbital basis set consisting of these orbitals (see Methods for details).

Figure 3(a) shows the orbital-resolved TB band structure without SOC terms. For comparison, the corresponding DFT band structure is also shown (dashed lines). The Wannier TB model successfully reproduces the bulk Dirac cones as well as the band inversion in the vicinity of the Fermi level, which are the two characteristic features of the Generalized Gradient Approximation (GGA) band structure within the scalar relativistic approximation ('no SOC'). To reproduce the Dirac node, however, we need to include hopping terms up to the third-nearest neighbors (up to ∼20 Å). We note that, compared to the DFT band structure, the location of the Dirac point in BZ is shifted toward (but not exactly at) the Y point regardless of the number of neighbors considered in the model. The details of the Hamiltonian and the corresponding TB parameters are provided in Methods.

Upon inclusion of SOC terms which preserve the time-reversal symmetry $\mathcal{T}$, glide mirror symmetry $\widetilde{M}_x$, glide screw $\widetilde{C}_{2x}$ symmetry, and therefore the effective inversion symmetry $\mathcal{I}$, the resulting TB Hamiltonian matrix is 8×8 and consists of three additional terms (see Sec. VI F). The corresponding TB band structure along with the DFT band structure (with SOC) is shown in Fig. 3(b). In both the TB and DFT band structures, each band is doubly degenerate. The fundamental gap of the minimal model is ∼53 meV, somewhat smaller than the DFT result. However, the band inversion around the Y point is reproduced reasonably well. Most importantly, the Wilson loop spectrum in Fig. 3(c) confirms that the minimal TB model captures the QSHI ground state.

In order to clarify the role of SOC in driving the QSHI phase in monolayer $TaRhTe_4$, we numerically/artificially tune the SOC strength in the four-orbital minimal model. Specifically, we considered the situation when the effective strength of SOC, λ, is only 5% and 10% of the value in the material-based minimal model, λ_0 (equivalently, in the minimal model with parameters tabulated in Table II). Figure 3(c) shows the

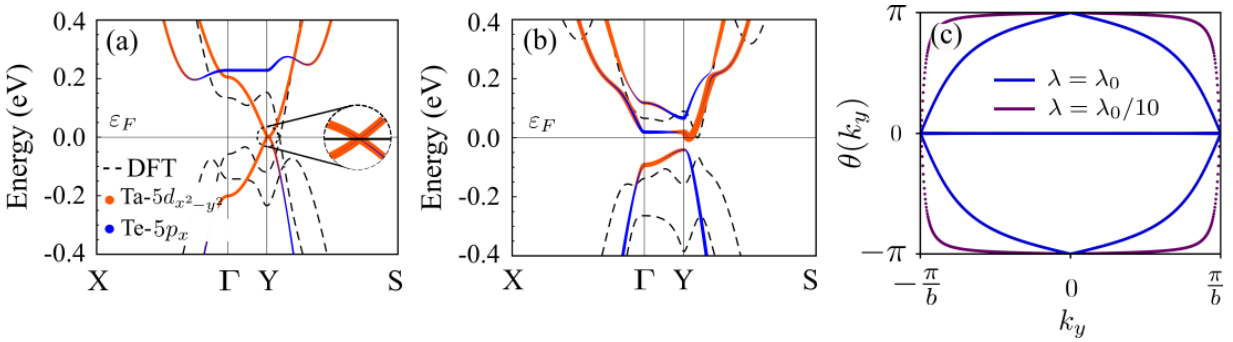

FIG. 3. TB model for monolayer $TaRhTe_4$. Band structures obtained from the four-orbital TB model for (a) without and (b) with SOC along with the orbital contributions. The DFT bands are shown with black dashed lines for comparison. (c) Wilson loop spectra for the TB model (blue curve), and for the model where the SOC terms are scaled down to 10% of the real values (purple color).

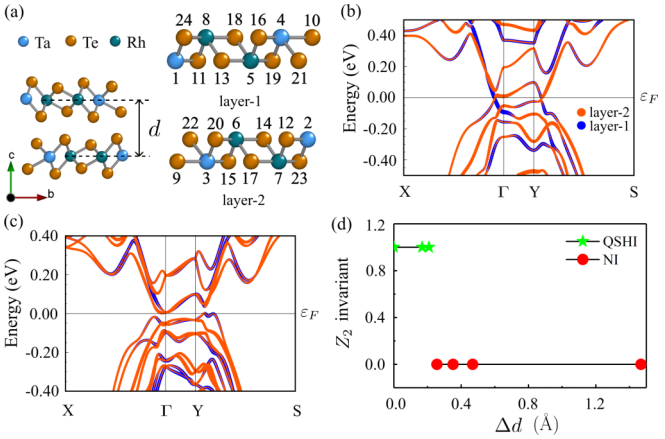

FIG. 4. Structure and electronic properties of bilayer $TaRhTe_4$. (a) Side view of AB stacking $TaRhTe_4$. For ease of discussion, all the atoms have been numbered. The interlayer distance is defined as d, where the equilibrium interlayer distance $d_0 = 6.58$ Å. (b) Layer resolved band structure of bilayer $TaRhTe_4$ without SOC. (c) Energy bands of bilayer $TaRhTe_4$ with SOC. (d) Topological $\mathcal{Z}_2$ invariant as a function of the interlayer distance Δd.

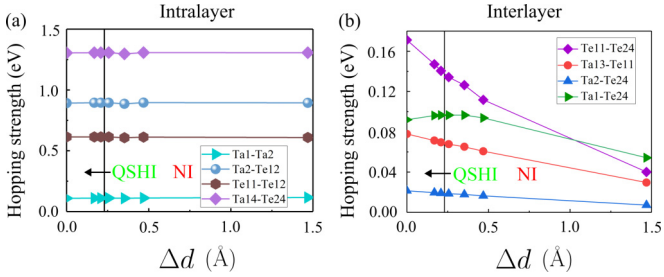

FIG. 5. Dominant (a) intralayer and (b) interlayer hopping strengths in bilayer $TaRhTe_4$ as a function of Δd. The atoms in the layer-1 and layer-2 of bilayer structure are marked by numbers in Fig. 4(a). The vertical black line represents the topological phase transition boundary between the QSHI and NI phases.

Wilson loops for the latter case, $\lambda/\lambda_0 = 0.1$. Remarkably, we find $\mathcal{Z}_2 = 1$ even in this case, which means that the role of SOC is not as important as band inversion, and even rather weak SOC can maintain the QSHI phase in the monolayer $TaRhTe_4$.

III. BILAYER SYSTEM

A bilayer $TaRhTe_4$ system was constructed from the bulk unit cell in a fashion similar to the monolayer (see Methods for details). The unit cell consists of two AB-stacked, as shown in Fig. 4(a). Compared to the monolayer, the bilayer breaks the screw symmetry due to the displacement between the layers in the $\mathbf{e}_x$-$\mathbf{e}_y$ plane. Thus, the effective inversion symmetry is also broken and the space group consists only of mirror reflection M_x.

A. Role of interlayer separation

Figure 4(b) shows the band structure of bilayer $TaRhTe_4$ with layer-resolved orbital contributions along a high-symmetry path for the scalar relativistic case. The highest-lying valence band N, where N is the number of valence electrons, and the lowest-lying conduction band $N + 1$ are quite close along Γ-X and Y-S but do not cross.

When SOC is included, bands are no longer doubly degenerate, as shown in Fig. 4(c). The ground state is a zero-gap semimetal with direct band gaps around the Γ point. The average value of the direct gap is ∼50 meV (min: ∼30 meV, max: ∼100 meV). In contrast to the monolayer case, the band degeneracy is lifted due to the lack of effective inversion symmetry.

Given its quasi-2D structure with two vdW-separated layers, we used the topological index $\mathcal{Z}_2 = (\nu_0; \nu_1\nu_2\nu_3)$ based on Wannier center evolution [63] (see Methods), the topology of the band structure was ascertained by calculating the $\mathcal{Z}_2$ topological invariant. We find $\mathcal{Z}_2 = (0; 001)$ for the bilayer $TaRhTe_4$ which indicates the presence of edge states on facets perpendicular to the layer direction, corresponding to a QSHI ground state. Therefore, the bilayer $TaRhTe_4$ also hosts a nontrivial topological ground state. Strictly speaking, this ground state is a WTI, but due to the quasi-2D structure of the bilayer, it behaves as a 2D QSHI. In SM Fig. S7, we provide an edge state spectrum of bilayer $TaRhTe_4$ in a nanoribbon geometry.

With increasing interlayer separation $d = d_0 + \Delta d$, where $d_0 = 6.58$ Å is the interlayer separation in the bulk 3D compound, a topological phase transition to a trivial insulator occurs at $\Delta d = 0.23$ Å ($\Delta d/d_0 = 3.5\%$; $d = 6.81$ Å); see Fig. 4(d). This behavior is similar to the Ir compound, $TaIrTe_4$, and has been attributed to the strong interlayer coupling [50].

Interestingly, in $TaRhTe_4$, the ground state is insensitive to the stacking pattern of the layers in the bilayer unit cell. We find that the AA-stacked bilayer, with no relative displacement in the $\mathbf{e}_x$-$\mathbf{e}_y$ plane between the layers, retains screw symmetry and inversion symmetry, and also hosts a QSH ground state. The AA-stacked $TaRhTe_4$ transitions to a trivial insulator when the interlayer distance exceeds 6.42 Å. Although AA-stacked structures are deemed unstable [31], efforts are being made to manipulate interlayer stacking in some transition metal dichalcogenides [64]. This is particularly relevant since ternary compositions offer greater flexibility in manipulating composition and structure. Additionally, this allows access to the QSH state in bilayer systems with different interlayer interactions [65].

B. Intralayer and interlayer hoppings

In order to gain further insights into the topological phase transition in bilayer $TaRhTe_4$, we analyze the dependence of intra- and interlayer hopping integrals on the interlayer distance based on a highly accurate 44-orbital Wannier model (see Methods for details). Figure 5(a) shows selected dominant intralayer hoppings of Ta-Ta, Ta-Te, and Te-Te. The hoppings between Ta and Te atoms are typically around 1 eV, while Ta-Ta hoppings are an order of magnitude smaller. As expected, the intralayer hoppings remain almost unchanged with increasing interlayer separation d.

In comparison, the dominant interlayer hoppings range between around 10 and 100 meV, as shown in Fig. 5(b). With increasing interlayer separation d, the orbital overlaps

decrease and eventually become zero as $\Delta d/d_0 \gg 1$. Some of these hoppings, in fact, vanish even at $\Delta d \approx 1.5$ Å ($\Delta d/d_0 \approx 18.6\%$). Evidently, the interlayer couplings are reasonably strong to drive the system into a QSHI phase and decay smoothly across the topological phase boundary.

The QSH state in bilayer $TaRhTe_4$ is somewhat counterintuitive, as coupling between the Dirac cones from each monolayer is expected to gap them out, rendering a trivial ground state. The large interlayer hoppings are a result of enhanced bandwidths of the monolayer densities of states. However, the QSHI phase is stabilized by the presence of additional band inversion between the layer-resolved orbital contributions around the Y point, as shown in Fig. 4(c). With increasing interlayer separation, the contribution of layer-1 to the topmost valence band decreases, while its contribution to the lowest valence band increases; the behavior of layer-2 is the opposite (see Fig. S5 for details [59]). Across the phase transition point, the energy gap near the Y point closes and reopens, with significant modifications in the band weight contributions from both layers. After crossing the phase boundary, the contributions of the vdW-separated layers tend to equalize in the conduction and valence band edges.

Furthermore, it would be expected that systems with an odd number of layers would be QSHIs akin to the monolayer $TaRhTe_4$. Remarkably, the QSHI bilayer systems imply that few-layer systems with an even number of layers per unit cell would likely also host a QSHI ground state.

More importantly, we find that the QSHI state in monolayer $TaRhTe_4$ is robust against strain values up to ∼13% (see SM [59]). This makes the monolayers a natural candidate for possible applications for typical substrates, such as hBN where an appropriate lattice orientation leads to strain values less than 5%.

We further obtain the exfoliation energies for both of them. It is found that the exfoliation energy for monolayer $TaRhTe_4$ is 2.85 meV/Å^2, while the energy for the bilayer system is 1.75 meV/Å^2 (see SM [59]). For comparison, we also computed the exfoliation energy for graphene in the same way as mentioned in the Methods for reference, and found it to be 1.3 meV/Å^2 comparable to the experimental data [66]. The exfoliation energy of bilayer $TaRhTe_4$ is comparable to that of graphene, while the energy of the monolayer system is about two times larger than that of graphene, rendering these systems particularly appealing for possible technological applications.

IV. TOPOLOGICAL PHASE TRANSITIONS: FROM BILAYER TO BULK

A. Weyl semimetal phase in 3D $TaRhTe_4$

The unit cell of the 3D $TaRhTe_4$ is structurally equivalent to stacked bilayers as shown in Fig. 1(a). We define the interbilayer distance as c and intrabilayer distance as d. The space group and symmetry of the 3D structure have been previously discussed. The band structure with SOC effects along high-symmetry paths is shown in SM Fig. S9. The top of the occupied band (band N where N is the number of valence electrons in the system, blue curve) leads to 3D hole pockets along Γ-X and Γ-Y while the band $N+1$ (red curve) for electron pocket around Γ.

TABLE I. Positions, chirality (χ), and energies of the Weyl points formed between bands N and $N+1$ in bulk $TaRhTe_4$, where N is the number of valence electrons. All WPs are four-fold degenerate, related by the symmetries C_{2z} and M_x.

	$(k_x, k_y, k_z)\frac{2\pi}{a}$	χ	E (meV)
W_1	(0.150553, 0.105029, 0)	−1	125.2
W_2	(0.019475, 0.098853, 0)	+1	−43.0
W_3	(0.025053, 0.066748, 0)	+1	−63.7

The DFT calculations confirm that 3D $TaRhTe_4$ is a Weyl semimetal [67], similar to 3D $TaIrTe_4$. Within GGA, we obtain three quartets of Weyl points (WPs) between the highest occupied band (blue curve) and the lowest unoccupied band (red curve). Moreover, all the WPs lie in the $k_z = 0$ plane. Table I lists the position and energy of these WPs alongside their chirality.

B. Phase diagram with intra- and interbilayer distance

We now turn our attention to possible topological phase transitions from a monolayer and bilayer QSHI to the 3D WSM phase in $TaRhTe_4$. This is achieved by tuning the intrabilayer ($d = d_0 + \Delta d$) and interbilayer distance ($c = c_0 + \Delta c$), where c_0 and d_0 represents the interlayer separation for the bulk 3D $TaRhTe_4$ [see the inset of Fig. 6(a)]. Several interesting possibilities emerge: (i) In the limit of $c, d \to \infty$, one would expect to recover the topology of the monolayer, while (ii) $c = d = c_0$ represents the bulk 3D system. (iii) $\Delta d = 0$, $\Delta c = \infty$ corresponds to a WTI since it can be understood as a stacking of bilayer $TaRhTe_4$ which is a QSHI, along the z axis. (iv) $\Delta c \neq \Delta d \neq 0$ represents a generic situation.

We consider a sizable range for the inter- and intralayer separation, up to $\Delta c/c_0 = \Delta d/d_0 = 51.7\%$. While not all points in the phase diagram may be experimentally achievable, a significant region is relevant for intercalated and/or exfoliated systems, for which the TPTs and their boundaries are not yet known. The phase diagram must be symmetric about the $c = d$ diagonal, so computing the ground state properties in the bottom triangular region of the $c = d$ phase diagram is sufficient.

The resulting phase diagram, shown in Fig. 6(a), is quite rich and consists of topological insulator (QSHI/WTI), WSM, and NI regions. Computations are carried out only in the bottom triangle of the phase diagram. All the computed structures are represented by filled circles. The phase boundaries are a guide to the eye and encompass the phase transitions discussed above.

For $\Delta c/c_0 = \Delta d/d_0 \gg 1$, the unit cell is equivalent to well separated noninteracting monolayers. The expected ground state is thus a QSHI. From computations of the 3D $\mathcal{Z}_2$ invariant of the considered largest value of $\Delta c/c_0 = \Delta d/d_0 = 51.7\%$, however, we find a trivial NI ground state. On the other hand, for $\Delta d = 0$ and $\Delta c/c_0 \gg 1$ corresponds to a bilayer system and the ground state is a WTI, as discussed earlier. For such a suitable but fixed $\Delta c/c_0$, varying Δd [Path I in Fig. 6(a)] leads to a topological phase transition between the WTI and the NI phase, i.e., from $\mathcal{Z}_2 = (0;001)$ to $\mathcal{Z}_2 = (0;000)$

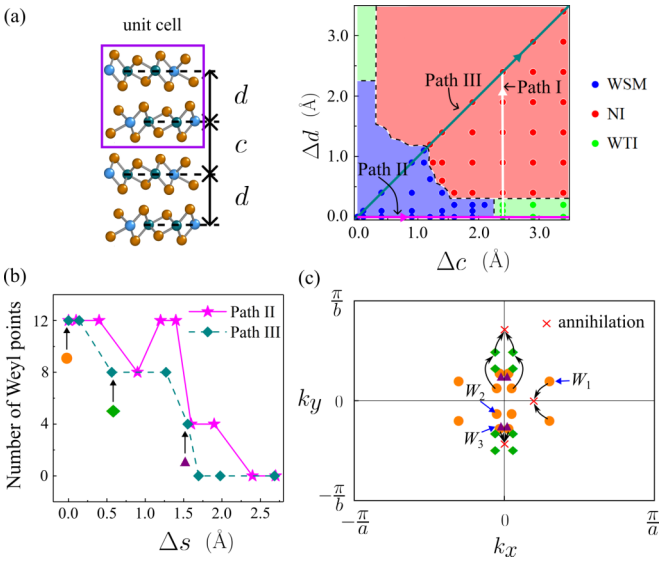

FIG. 6. (a) Left panel: Phase diagram of 3D $TaRhTe_4$ in the c-d plane. Ground state at each point (filled circles) is obtained from DFT calculation. The black dashed curves are a guide to the eye for the phase boundaries. Paths I, II, and III highlight the WSM-WTI, WSM-NI, and WTI-NI phase boundaries, respectively. Right panel: side view of $TaRhTe_4$ with two unit cells, where the interbilayer distance $c = c_0 + \Delta c$ and the intrabilayer distance $d = d_0 + \Delta d$. (b) The number of WPs as a function of Δs along Path II and Path III, where $\Delta s = \sqrt{\Delta c^2 + \Delta d^2}$. (c) The coordinates of WPs in BZ selected from Path III of the phase diagram. The corresponding chosen points are marked in (b). The red crosses represent the positions in the BZ where the WPs annihilate.

for $\Delta c = 2.4$ Å and $\Delta d = 0.23$ Å, i.e., $\Delta c/c_0 = 36.5\%$ and $\Delta d/d_0 = 3.5\%$, and was discussed above in detail.

Similarly, for $\Delta c = \Delta d = 0$, corresponding to the bulk $TaRhTe_4$, the ground state is a WSM. Keeping $\Delta d = 0$ fixed, and increasing $\Delta c/c_0$ corresponds to a structural phase transition from the bulk 3D structure to the AB-stacked bilayer $TaRhTe_4$. By the same token, a topological phase transition from the WSM phase to the WTI ground state is found, as shown in Path II along $\Delta d = 0$.

The WSM phase extends to regions of small Δc and Δd, whereas WTI is located in the area with large Δc but small Δd. With large $\Delta c/c_0$ and $\Delta d/d_0$, the $TaRhTe_4$ system becomes a NI. Naturally, band gap opens when the phase transitions of WSM-WTI and WSM-NI occur. At the same time, the interbilayer and intrabilayer separation induces the creation and annihilation of WPs in the WSM phase.

To further illustrate these topological phase transitions, we consider paths II and III which, respectively, highlight the WSM-WTI and WSM-NI topological phase transitions. Figure 6(b) shows the number of Weyl points as a function of Δs along these paths. Because of the time-reversal symmetry, Weyl nodes are always created and annihilated as quartets.

Along Path II, the number of WPs in $TaRhTe_4$ decreases to four before the phase transition, and completely annihilated at around $\Delta s = \sqrt{\Delta c^2 + \Delta d^2} \approx 2$ Å. When $\Delta s = 0.9$ Å, the number of WPs decreases from 12 to eight, as eight WPs annihilate and four new WPs are created (not show). Similar behavior can be observed along Path III. A band gap opens up already at around $\Delta s \approx 1.7$ Å. Due to $c = d$, all symmetries in the equilibrium 3D structure of bulk $TaRhTe_4$ are preserved. Therefore, all the Weyl points are still constrained in $k_z = 0$ plane. In Fig. 6(c), we show the evolution of the WPs along path III. For brevity, we depict the coordinates of WPs for selected values of Δs. The WPs for $\Delta s = 0$ are denoted by orange dots, and their positions in the BZ are listed in Table I. As Δs increases, the quartet W_1 moves continuously closer to the origin and eventually annihilates each other on the k_x axis. Concurrently, the WPs W_2 and W_3 move along the k_y axis increasing their relative separations. At $\Delta s = 0.5$ Å, only two quartets (W_2 and W_3) survive, with their positions in the BZ shown by green diamonds. Further increasing Δs creates additional WPs close to the k_x axis, which annihilate rather quickly with small changes in Δs (not shown). Simultaneously, both quartet W_2 and W_3 get annihilated. Increasing Δs even further to $\Delta s = 1.7$ Å creates a new quartet of WPs close to $k_x = 0$ axis, shown by purple triangles that eventually annihilate each other at the phase boundary between the WSM and the NI states.

V. CONCLUSION AND OUTLOOK

Our investigation of the monolayer, bilayer, and bulk $TaRhTe_4$ systems using DFT reveals several interesting and important aspects of layered vdW tellurides in general, and $TaRhTe_4$ in particular.

First, monolayer $TaRhTe_4$ is a QSHI with a 65 meV bulk gap, suggesting its viability for room temperature applications. Additionally, the minimal four-orbital tight-binding model presented here will enable further investigations of disorder and geometric effects in realistic samples.

Second, our analysis of the inter- and intralayer TB parameters clarifies that even though the bilayer is vdW separated, it effectively exhibits a QSH effect. The presence of the QSHI phase in both monolayer and bilayer, as well as the insensitivity of the QSHI ground state to the stacking pattern in the bilayer, suggests that even few-layer $TaRhTe_4$ systems would also be QSHIs. This may have interesting implications for several related compositions and compounds.

Third, and perhaps most importantly, a rich phase diagram containing QSHI/WTI, WSM, and NI phases is obtained by varying the interlayer and interbilayer separations, comprehensively covering a vast majority of possible realistic situations under different synthesis conditions.

These insights are easily extendable not only to multi-/few-layer $TaRhTe_4$, but also to binary and ternary tellurides in general, and to intercalated and exfoliated tellurides in particular. Moreover, the higher degree of control offered by ternary compounds in terms of their composition and structure compared to their binary counterparts suggests that our findings will likely significantly impact the field of 2D chalcogenides. This will not only drive future theoretical and experimental investigations but also open up new avenues for quantum devices.

VI. METHODS

A. Crystal structures

The bulk crystal structure consists of four formula units and two vdW separated layers per unit cell. The lattice

constants are $a = 3.76$ Å, $b = 12.55$ Å, and $c = 13.17$ Å [52]. The interlayer separation is $c_0 = 6.58$ Å. The optimized atomic positions were used while the lattice constants were kept fixed at experimental values [52].

Monolayer $TaRhTe_4$ was constructed from the bulk unit cell by inserting a large vacuum between the two layers in the bulk unit cell. It was found that a vacuum $\gtrsim$15 Å does not influence the electronic properties of the monolayer. The atomic positions of the monolayer structure were first optimized under $Pmn2_1$ symmetry such that the force on each atom is less than 1 meV/Å. Then the lattice constants were tuned to minimize the total energy of the system. Finally, the atomic positions were optimized again under the new lattice constants. The in-plane lattice parameters are $a = 3.72$ Å and $b = 12.42$ Å, which are slightly smaller than bulk values. The electronic bands of the final structure match the results by using the structure from Materials Cloud [68]. For comparison, the energy bands with optimized atomic positions but unoptimized lattice constants are presented in the SM [59].

Similarly, bilayer $TaRhTe_4$ systems were prepared by inserting a large vacuum between the bilayers in the bulk unit cell. For the bilayer system with an intrabilayer distance equal to the interlayer separation in the bulk 3D system, but a large interbilayer distance, the atomic positions were optimized with a force threshold of 1 meV/Å for each atom. Other bilayer structures with different intrabilayer separations were realized by inserting the vacuum directly in the optimized structure. The resulting crystal structures for monolayer as well as bilayer systems are presented in the SM [59].

B. DFT calculations

The DFT calculations were carried out for monolayer, bilayer and bulk $TaRhTe_4$ systems using the Full-Potential Local-Orbital (FPLO) code [69], version 18.57 [70]. The Perdew-Burke-Ernzerhof implementation [71] of the GGA was employed in all cases. For the numerical integration of monolayers and bilayers, we used a k mesh with $(20 \times 10 \times 1)$ intervals in the BZ, and a k mesh with $(20 \times 10 \times 10)$ intervals for bulk $TaRhTe_4$. The linear tetrahedron method was used for the numerical integration in the Brillouin zone. As applicable, the 'no SOC' was used, while the SOC effects were included via the 4-spinor formalism as implemented in the FPLO code.

C. Topological electronic properties

For the monolayer insulators, a highly accurate maximally projected Wannier model was constructed and was used for the computation of the topological properties. It was constructed by projecting the band structure onto a subset of atomic-like basis functions (Wannier functions) within a given energy window. We focused on a set of isolated bands across the Fermi energy, lying between -6.5 eV and $+2.3$ eV, which have dominant contributions from the Ta-5d orbitals, Rh-4d orbitals, and Te-5p orbitals.

The topology of the band structure was determined by calculating the $\mathcal{Z}_2$ index with via the Wilson loop method (own code) [61]. The sensitivity of the ground state to the Te positions was explicitly checked by considering an inversion symmetric unit cell with relaxed atomic positions for which the $\mathcal{Z}_2$ index matches with the corresponding value obtained via the method of Wannier center evolution provided by FPLO [63], suggesting the topology is robust against perturbations to Te positions.

The edge state spectra were obtained by computing the bulk projected bands using nanoribbon geometry as implemented in the PYFPLO module of the FPLO code. Two blocks of unit cells are used as ribbon width in all semislab calculations. Two hundred points were sampled across the energy window spanning $[-0.15, 0.15]$ eV.

For the bilayers, with a direct gap throughout the BZ, the topological properties were ascertained from the $\mathcal{Z}_2 = (\nu_0; \nu_1\nu_2\nu_3)$ index for the 3D systems, obtained via the Wannier center evolution algorithm as implemented in the FPLO code.

The Wannier tight-binding model comprises the Ta-5d orbitals, Rh-4d orbitals, and Te-5p orbitals with energy window lying between -7.0 eV and $+2.5$ eV. The basis set for the Wannier projections consists of 88 orbitals for the scalar relativistic case ('no SOC'). Correspondingly, the basis of Wannier functions involved 176 orbitals when spin-orbit interactions were considered. Because varying the interlayer separations does not significantly change the distribution of bands, the energy window was kept between -7.0 eV and $+2.5$ eV in all bilayer computations.

For the bulk $TaRhTe_4$, on the other hand, the ground state is semimetallic. To study its underlying topology of the electronic structure, we constructed a Wannier model projecting the band structure onto Wannier functions for the isolated manifold of bands between -6.5 eV and $+4.3$ eV, which have dominant contributions from the Ta-5d, Rh-4d, 5s, and Te-5p orbitals. Therefore, the basis set for the Wannier projections consists of 92 orbitals for the scalar relativistic case. Correspondingly, the basis of Wannier functions involved 184 orbitals when spin-orbit interactions were considered. The WPs were obtained and confirmed by computing the Chern numbers as implemented in the PYFPLO module of the FPLO code, and outlined in Ref. [44].

D. Exfoliation energy

In order to estimate the energy cost of exfoliating monolayer and bilayer $TaRhTe_4$ from a real bulk system, we calculated their exfoliation energies. We define exfoliation energy as the energy needed to completely detach all the layers in the bulk unit cell. It is worth noting that in certain studies [72,73], exfoliation energy is alternatively defined as the energy expended in removing the top layer from the surface of a bulk crystal. Thereby, we compute the total energy of the bulk $TaRhTe_4$ as a function of the intrabilayer distance d and interbilayer distance c, and obtain the difference from the energy of the equilibrium structure. For the bilayer system, we vary the interlayer distance c only. To arrive at the monolayer limit, we vary both the intrabilayer and interbilayer distances at the same time. For these calculations, we use a k mesh with $(20 \times 20 \times 10)$ intervals in the BZ. Because there are two layers per unit cell, we divide the energy by four times the surface area $(3.76 \times 12.55$ Å$^2)$ of unit cell as the final monolayer exfoliation energy, whereas we divide two times surface area as the final bilayer exfoliation energy. As a benchmark, we

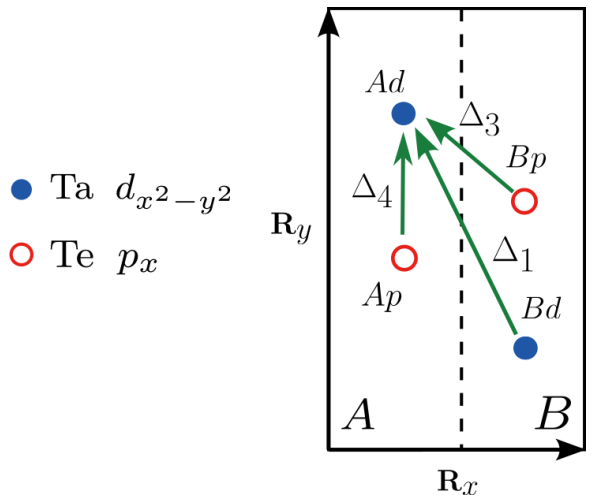

FIG. 7. Reduced four-site unit cell for the tight-binding model with sublattices A and B. The arrows depict the hopping terms (s_0) and the (spin-orbit coupling) SOC terms (s_z) of the model. The lattice vectors are labeled by $\mathbf{R}_x$ and $\mathbf{R}_y$.

also obtain the exfoliation energy for graphite. The situation of graphene is the same as that of the monolayer, i.e., we divide the energy by four times the surface area to obtain the exfoliation energy.

E. Phonon spectrum

We calculate the phonon spectrum of monolayer $TaRhTe_4$ by using the Vienna *ab initio* Simulation Package (VASP) [74], version 5.4.2, and the PHONOPY package [75], version 2.20.0. The second-order harmonic interatomic force constants are calculated by the density-functional perturbation theory with a $(2 \times 2 \times 1)$ supercell and a $(5 \times 2 \times 1)$ k mesh, employing projector augmented-wave pseudopotential [76], where the cutoff energy is set as 500 eV. In the SM [59], we show the phonon spectrum of monolayer $TaRhTe_4$.

F. Minimal TB model for monolayer $TaRhTe_4$

For the monolayer, a four-orbital TB model was also obtained, starting from the symmetry-based Hamiltonian in Ref. [57] and considering long-range hopping terms, up to ∼20 Å. According to Fig. 7, we label all the hoppings in real space included in the TB model with the following notation for distances up to the third-nearest neighbors in terms of the intracell distances and lattice vectors:

$$\begin{aligned}
\mathbf{r}_0 &= -\Delta_4, \quad \mathbf{r}_{0x} = -(\Delta_4 + \mathbf{R}_x),\\
\mathbf{r}_{px} &= \mathbf{R}_x, \quad \mathbf{r}_{dx} = \mathbf{R}_x,\\
\mathbf{r}_{pAB} &= \Delta_2 + \mathbf{R}_x, \quad \mathbf{r}_{pABx} = \Delta_2 + 2\mathbf{R}_x,\\
\mathbf{r}_{dAB} &= -\Delta_1, \quad \mathbf{r}_{dABx} = \mathbf{R}_x - \Delta_1,\\
\mathbf{r}_{dABx1} &= 2\mathbf{R}_x - \Delta_1, \quad \mathbf{r}_{dABy} = \mathbf{R}_y - \Delta_1,\\
\mathbf{r}_{dABy1} &= \mathbf{R}_x + \mathbf{R}_y - \Delta_1, \quad \mathbf{r}_{dABy2} = 2\mathbf{R}_x + \mathbf{R}_y - \Delta_1,\\
\mathbf{r}_{0AB} &= \Delta_3, \quad \mathbf{r}_{0ABx} = 2\mathbf{R}_x + \Delta_3,\\
\mathbf{r}_{0ABx1} &= 3\mathbf{R}_x + \Delta_3. \qquad (1)
\end{aligned}$$

Here, the vectors are defined as $\Delta_1 = \mathbf{r}_{Ad} - \mathbf{r}_{Bd}$, $\Delta_2 = \mathbf{r}_{Ap} - \mathbf{r}_{Bp}$, $\Delta_3 = \mathbf{r}_{Ad} - \mathbf{r}_{Bp}$, and $\Delta_4 = \mathbf{r}_{Ad} - \mathbf{r}_{Ap}$ in unit cell, where the vector $\mathbf{r}_{cl}$ denotes the position of the corresponding lattice site, associated with an orbital l in sublattice c, in the unit cell. We list the coordinates of vectors as $\mathbf{r}_{Ad} = (-0.25a, 0.16b)$, $\mathbf{r}_{Bp} = (0.25a, 0.044b)$, $\mathbf{r}_{Ap} = (-0.25a, -0.044b)$, and $\mathbf{r}_{Bd} = (0.25a, -0.16b)$.

The Hamiltonian without SOC is expressed as

$$\begin{aligned}
H_0 = &\left[\frac{\mu_p}{2} + t_{px}\cos(k_x a)\right]\Gamma_1^- + \left[\frac{\mu_d}{2} + t_{dx}\cos(k_x a)\right]\Gamma_1^+\\
&+ [t_{dAB}(1 + e^{ik_x a}) + t_{dABx}(e^{-ik_x a} + e^{2ik_x a})\\
&+ t_{dABx1}(e^{-2ik_x a} + e^{3ik_x a}) + t_{dABy}e^{-ik_y b}(1 + e^{ik_x a})\\
&+ t_{dABy1}e^{-ik_y b}(e^{-ik_x a} + e^{2ik_x a})\\
&+ t_{dABy2}e^{-ik_y b}(e^{-2ik_x a} + e^{3ik_x a})]e^{i\mathbf{k}\cdot\Delta_1}\Gamma_2^+\\
&+ [t_{pAB}(1 + e^{ik_x a}) + t_{pABx}(e^{-ik_x a} + e^{2ik_x a})]e^{i\mathbf{k}\cdot\Delta_2}\Gamma_2^-\\
&+ [t_{0AB}(1 - e^{ik_x a}) + t_{0ABx}(e^{-ik_x a} - e^{2ik_x a})\\
&+ t_{0ABx1}(e^{-2ik_x a} - e^{3ik_x a})]e^{i\mathbf{k}\cdot\Delta_3}\Gamma_3\\
&- 2it_{0x}\sin(k_x a)[e^{i\mathbf{k}\cdot\Delta_4}\Gamma_4^- + e^{-i\mathbf{k}\cdot\Delta_4}\Gamma_4^+] + \text{H.c.} \qquad (2)
\end{aligned}$$

The 4×4 matrices Γ_i are linear combinations of products $\tau_i\sigma_i$ of Pauli matrices and Δ_i are vectors corresponding to interatomic distances and are defined below.

Specifically, the hopping parameters in the Hamiltonian are defined as

$$t(\mathbf{r}_i) = \langle\phi_l(\mathbf{r}) \mid \hat{H} \mid \phi_l(\mathbf{r} - \mathbf{r}_i)\rangle, \qquad (3)$$

where $\phi_l(\mathbf{r})$ is the maximally localized Wannier orbitals. The matrices Γ_i have the form:

$$\Gamma_0 = \tau_0\sigma_0, \qquad (4)$$

$$\Gamma_1^{\pm} = \frac{\tau_0}{2}(\sigma_0 \pm \sigma_3), \qquad (5)$$

$$\Gamma_2^{\pm} = \tfrac{1}{4}(\tau_1 + i\tau_2)(\sigma_0 \pm \sigma_3), \qquad (6)$$

$$\Gamma_3 = \tfrac{1}{2}(\tau_1 + i\tau_2)i\sigma_2, \qquad (7)$$

$$\Gamma_4^{\pm} = \tfrac{1}{4}(\tau_0 \pm \tau_3)(\sigma_1 + i\sigma_2), \qquad (8)$$

$$\Gamma_5^{\pm} = \frac{\tau_3}{2}(\sigma_0 \pm \sigma_3), \qquad (9)$$

$$\Gamma_6 = \tfrac{1}{2}(\tau_1 + i\tau_2)\sigma_1, \qquad (10)$$

where the matrices $\tau_j\sigma_i$ are products of Pauli matrices acting in orbital space with respect to the basis $\{d_{\mathbf{k}Ads}, d_{\mathbf{k}Aps}, d_{\mathbf{k}Bds}, d_{\mathbf{k}Bps}\}$, where $d_{\mathbf{k}cls}$ annihilates an electron with momentum $\mathbf{k}$, spin-S_z eigenvalue $s = \uparrow, \downarrow$ and orbital $l = p, d$ (Te, Ta) in sublattice $c = A, B$. In other words, τ_j acts on the sublattice degree of freedom and σ_i acts on the orbital degree of freedom.

When taking into account SOC, the minimal model is constructed by localized Wannier orbitals of the Ta-d and Te-p orbitals along with the spin degrees of freedom, which gives rise to an eight-orbital model. Based on the minimal tight-binding model without SOC, we include spin-orbit coupling terms that preserve: time-reversal symmetry $\mathcal{T}$, glide

TABLE II. Tight-binding model parameters of the four-orbital minimal model for monolayer $TaRhTe_4$. The model parameters correspond to Eqs. (2) and (11) and are shown in Fig. 1(d).

Parameter	Value (meV)	Parameter	Value (meV)
A. TB model without SOC H_0			
μ_p	590	t_{dABx1}	30
μ_d	−2070	t_{dABy}	−26
t_{px}	940	t_{dABy1}	−11
t_{dx}	−290	t_{dABy2}	−15
t_{pAB}	240	t_{0AB}	−120
t_{pABx}	−38	t_{0ABx}	−81
t_{dAB}	−110	t_{0ABx1}	−26
t_{dABx}	27	t_{0x}	57
B. SOC terms H_{SOC}			
λ^z_{0AB}	16.8	λ^z_{px}	7.5
λ^z_{dx}	7.1	λ^z_0	9.8

mirror symmetry $\widetilde{M}_x$, glide screw $\widetilde{C}_{2x}$ symmetry, and inversion $\mathcal{I}$ symmetry. In the basis of the Hamiltonian in Eq. (2), the matrix representations of the symmetry operations are $\hat{\mathcal{T}} = is_y\Gamma_0 K$ with complex conjugation K, $\hat{\mathcal{I}} = s_0\tau_1\sigma_3$, and $\hat{M}_x = is_x\tau_0\sigma_3$ for the nontranslational component of $\widetilde{M}_x$. By taking the hopping parameters ($\geqslant$0.014) eV from the Wannier fit result, the Bloch Hamiltonian of the final tight-binding model with SOC is $H(\mathbf{k}) = s_0H_0(\mathbf{k}) + H_{SOC}(\mathbf{k})$, with

$$\begin{aligned} H_{SOC} = {} & \lambda^z_{dx}s_z\sin(ak_x)\Gamma^+_5 + \lambda^z_{px}s_z\sin(ak_x)\Gamma^-_5 \\ & - i\lambda^z_{0AB}s_z(1+e^{iak_x})e^{i\mathbf{k}\cdot\Delta_3}\Gamma_6 \\ & - i\lambda^z_0 s_z(e^{i\mathbf{k}\cdot\Delta_4}\Gamma^+_4 - e^{-i\mathbf{k}\cdot\Delta_4}\Gamma^-_4) + \text{H.c.} \end{aligned} \tag{11}$$

where s_i are Pauli matrices acting in spin space and s_0 is the 2×2 identity matrix. Parameter values in Eqs. (2) and (11) are listed in Table II.

ACKNOWLEDGMENTS

X.Z. thanks Hui Liu, Ion Cosma Fulga, and Mengli Hu for helpful discussions and Ulrike Nitzsche for technical assistance. R.R. acknowledges helpful discussions with Anupam Roy. We acknowledge financial support from German Forschungsgemeinschaft (DFG, German Research Foundation) via SFB 1143 (Project No. 247310070) and under Germany's Excellence Strategy through Würzburg-Dresden Cluster of Excellence on Complexity and Topology in Quantum Matter - *ct.qmat* (EXC 2147, Project No. 390858490).

[1] F. D. M. Haldane, Nobel lecture: Topological quantum matter, Rev. Mod. Phys. **89**, 040502 (2017).
[2] M. Z. Hasan and C. L. Kane, *Colloquium:* Topological insulators, Rev. Mod. Phys. **82**, 3045 (2010).
[3] J. E. Moore, The birth of topological insulators, Nature (London) **464**, 194 (2010).
[4] X. Wan, A. M. Turner, A. Vishwanath, and S. Y. Savrasov, Topological semimetal and Fermi-arc surface states in the electronic structure of pyrochlore iridates, Phys. Rev. B **83**, 205101 (2011).
[5] H. Weng, C. Fang, Z. Fang, B. A. Bernevig, and X. Dai, Weyl semimetal phase in noncentrosymmetric transition-metal monophosphides, Phys. Rev. X **5**, 011029 (2015).
[6] X.-L. Qi and S.-C. Zhang, Topological insulators and superconductors, Rev. Mod. Phys. **83**, 1057 (2011).
[7] W.-F. Tsai, C.-Y. Huang, T.-R. Chang, H. Lin, H.-T. Jeng, and A. Bansil, Gated silicene as a tunable source of nearly 100% spin-polarized electrons, Nat. Commun. **4**, 1500 (2013).
[8] F. de Juan, A. G. Grushin, T. Morimoto, and J. E. Moore, Quantized circular photogalvanic effect in Weyl semimetals, Nat. Commun. **8**, 15995 (2017).
[9] Q. L. He, T. L. Hughes, N. P. Armitage, Y. Tokura, and K. L. Wang, Topological spintronics and magnetoelectronics, Nat. Mater. **21**, 15 (2022).
[10] T. Fukui and Y. Hatsugai, Topological aspects of the quantum spin-Hall effect in graphene: Z_2 topological order and spin Chern number, Phys. Rev. B **75**, 121403(R) (2007).
[11] L. Fu and C. L. Kane, Topological insulators with inversion symmetry, Phys. Rev. B **76**, 045302 (2007).
[12] A. P. Schnyder, S. Ryu, A. Furusaki, and A. W. W. Ludwig, Classification of topological insulators and superconductors in three spatial dimensions, Phys. Rev. B **78**, 195125 (2008).
[13] L. Fu and C. L. Kane, Time reversal polarization and a Z_2 adiabatic spin pump, Phys. Rev. B **74**, 195312 (2006).
[14] C. L. Kane and E. J. Mele, Quantum spin Hall effect in graphene, Phys. Rev. Lett. **95**, 226801 (2005).
[15] C. L. Kane and E. J. Mele, Z_2 topological order and the quantum spin Hall effect, Phys. Rev. Lett. **95**, 146802 (2005).
[16] R. Roy, Z_2 classification of quantum spin Hall systems: An approach using time-reversal invariance, Phys. Rev. B **79**, 195321 (2009).
[17] X. Qian, J. Liu, L. Fu, and J. Li, Quantum spin Hall effect in two-dimensional transition metal dichalcogenides, Science **346**, 1344 (2014).
[18] L. Fu, C. L. Kane, and E. J. Mele, Topological insulators in three dimensions, Phys. Rev. Lett. **98**, 106803 (2007).
[19] J. E. Moore and L. Balents, Topological invariants of time-reversal-invariant band structures, Phys. Rev. B **75**, 121306(R) (2007).
[20] D. Hsieh, D. Qian, L. Wray, Y. Xia, Y. S. Hor, R. J. Cava, and M. Z. Hasan, A topological Dirac insulator in a quantum spin Hall phase, Nature (London) **452**, 970 (2008).
[21] Z. Ringel, Y. E. Kraus, and A. Stern, Strong side of weak topological insulators, Phys. Rev. B **86**, 045102 (2012).
[22] Z. Fan, Q.-F. Liang, Y. B. Chen, S.-H. Yao, and J. Zhou, Transition between strong and weak topological insulator in $ZrTe_4$ and $HfTe_5$, Sci. Rep. **7**, 45667 (2017).
[23] C.-X. Liu, X.-L. Qi, and S.-C. Zhang, Half quantum spin Hall effect on the surface of weak topological insulators, Physica E **44**, 906 (2012).
[24] A. A. Soluyanov, D. Gresch, Z. Wang, Q. Wu, M. Troyer, X. Dai, and B. A. Bernevig, Type-II Weyl semimetals, Nature (London) **527**, 495 (2015).
[25] A. A. Burkov and L. Balents, Weyl semimetal in a topological insulator multilayer, Phys. Rev. Lett. **107**, 127205 (2011).

[26] B. Q. Lv, T. Qian, and H. Ding, Experimental perspective on three-dimensional topological semimetals, Rev. Mod. Phys. **93**, 025002 (2021).

[27] N. P. Armitage, E. J. Mele, and A. Vishwanath, Weyl and Dirac semimetals in three-dimensional solids, Rev. Mod. Phys. **90**, 015001 (2018).

[28] S. Jia, S.-Y. Xu, and M. Z. Hasan, Weyl semimetals, Fermi arcs and chiral anomalies, Nat. Mater. **15**, 1140 (2016).

[29] S.-Y. Xu, C. Liu, S. K. Kushwaha, R. Sankar, J. W. Krizan, I. Belopolski, M. Neupane, G. Bian, N. Alidoust, T.-R. Chang, H.-T. Jeng, C.-Y. Huang, W.-F. Tsai, H. Lin, P. P. Shibayev, F.-C. Chou, R. J. Cava, and M. Z. Hasan, Observation of Fermi arc surface states in a topological metal, Science **347**, 294 (2015).

[30] B. Q. Lv, S. Muff, T. Qian, Z. D. Song, S. M. Nie, N. Xu, P. Richard, C. E. Matt, N. C. Plumb, L. X. Zhao, G. F. Chen, Z. Fang, X. Dai, J. H. Dil, J. Mesot, M. Shi, H. M. Weng, and H. Ding, Observation of Fermi-arc spin texture in TaAs, Phys. Rev. Lett. **115**, 217601 (2015).

[31] L. Muechler, A. Alexandradinata, T. Neupert, and R. Car, Topological nonsymmorphic metals from band inversion, Phys. Rev. X **6**, 041069 (2016).

[32] H. Zhang, C.-X. Liu, X.-L. Qi, X. Dai, Z. Fang, and S.-C. Zhang, Topological insulators in Bi_2Se_3, Bi_2Te_3 and Sb_2Te_3 with a single Dirac cone on the surface, Nat. Phys. **5**, 438 (2009).

[33] Y. Xia, D. Qian, D. Hsieh, L. Wray, A. Pal, H. Lin, A. Bansil, D. Grauer, Y. S. Hor, R. J. Cava, and M. Z. Hasan, Observation of a large-gap topological-insulator class with a single Dirac cone on the surface, Nat. Phys. **5**, 398 (2009).

[34] D. Hsieh, Y. Xia, D. Qian, L. Wray, J. H. Dil, F. Meier, J. Osterwalder, L. Patthey, J. G. Checkelsky, N. P. Ong, A. V. Fedorov, H. Lin, A. Bansil, D. Grauer, Y. S. Hor, R. J. Cava, and M. Z. Hasan, A tunable topological insulator in the spin helical Dirac transport regime, Nature (London) **460**, 1101 (2009).

[35] Y. L. Chen, J. G. Analytis, J.-H. Chu, Z. K. Liu, S.-K. Mo, X. L. Qi, H. J. Zhang, D. H. Lu, X. Dai, Z. Fang, S. C. Zhang, I. R. Fisher, Z. Hussain, and Z.-X. Shen, Experimental realization of a three-dimensional topological insulator, Bi_2Te_3, Science **325**, 178 (2009).

[36] B. Rasche, A. Isaeva, M. Ruck, S. Borisenko, V. Zabolotnyy, B. Büchner, K. Koepernik, C. Ortix, M. Richter, and J. van den Brink, Stacked topological insulator built from bismuth-based graphene sheet analogues, Nat. Mater. **12**, 422 (2013).

[37] E. Carrillo-Aravena, K. Finzel, R. Ray, M. Richter, T. Heider, I. Cojocariu, D. Baranowski, V. Feyer, L. Plucinski, M. Gruschwitz, C. Tegenkamp, and M. Ruck, $Bi_{12}Rh_3Cu_2I_5$: A 3D weak topological insulator with monolayer spacers and independent transport channels, Phys. Status Solidi B **259**, 2100447 (2022).

[38] B. Q. Lv, H. M. Weng, B. B. Fu, X. P. Wang, H. Miao, J. Ma, P. Richard, X. C. Huang, L. X. Zhao, G. F. Chen, Z. Fang, X. Dai, T. Qian, and H. Ding, Experimental discovery of Weyl semimetal TaAs, Phys. Rev. X **5**, 031013 (2015).

[39] B. Q. Lv, N. Xu, H. M. Weng, J. Z. Ma, P. Richard, X. C. Huang, L. X. Zhao, G. F. Chen, C. E. Matt, F. Bisti, V. N. Strocov, J. Mesot, Z. Fang, X. Dai, T. Qian, M. Shi, and H. Ding, Observation of Weyl nodes in TaAs, Nat. Phys. **11**, 724 (2015).

[40] P. Li, Y. Wen, X. He, Q. Zhang, C. Xia, Z.-M. Yu, S. A. Yang, Z. Zhu, H. N. Alshareef, and X.-X. Zhang, Evidence for topological type-II Weyl semimetal WTe_2, Nat. Commun. **8**, 2150 (2017).

[41] Y. Wu, D. Mou, N. H. Jo, K. Sun, L. Huang, S. L. Bud'ko, P. C. Canfield, and A. Kaminski, Observation of Fermi arcs in the type-II Weyl semimetal candidate WTe_2, Phys. Rev. B **94**, 121113(R) (2016).

[42] K. Deng, G. Wan, P. Deng, K. Zhang, S. Ding, E. Wang, M. Yan, H. Huang, H. Zhang, Z. Xu, J. Denlinger, A. Fedorov, H. Yang, W. Duan, H. Yao, Y. Wu, S. Fan, H. Zhang, X. Chen, and S. Zhou, Experimental observation of topological Fermi arcs in type-II Weyl semimetal $MoTe_2$, Nat. Phys. **12**, 1105 (2016).

[43] J. Jiang, Z. K. Liu, Y. Sun, H. F. Yang, C. R. Rajamathi, Y. P. Qi, L. X. Yang, C. Chen, H. Peng, C.-C. Hwang, S. Z. Sun, S.-K. Mo, I. Vobornik, J. Fujii, S. S. P. Parkin, C. Felser, B. H. Yan, and Y. L. Chen, Signature of type-II Weyl semimetal phase in $MoTe_2$, Nat. Commun. **8**, 13973 (2017).

[44] K. Koepernik, D. Kasinathan, D. V. Efremov, S. Khim, S. Borisenko, B. Büchner, and J. van den Brink, $TaIrTe_4$: A ternary type-II Weyl semimetal, Phys. Rev. B **93**, 201101(R) (2016).

[45] E. Haubold, K. Koepernik, D. Efremov, S. Khim, A. Fedorov, Y. Kushnirenko, J. van den Brink, S. Wurmehl, B. Büchner, T. K. Kim, M. Hoesch, K. Sumida, K. Taguchi, T. Yoshikawa, A. Kimura, T. Okuda, and S. V. Borisenko, Experimental realization of type-II Weyl state in noncentrosymmetric $TaIrTe_4$, Phys. Rev. B **95**, 241108(R) (2017).

[46] M. M. Otrokov, I. P. Rusinov, M. Blanco-Rey, M. Hoffmann, A. Yu. Vyazovskaya, S. V. Eremeev, A. Ernst, P. M. Echenique, A. Arnau, and E. V. Chulkov, Unique thickness-dependent properties of the van der Waals interlayer antiferromagnet $MnBi_2Te_4$ films, Phys. Rev. Lett. **122**, 107202 (2019).

[47] B. Huang, G. Clark, E. Navarro-Moratalla, D. R. Klein, R. Cheng, K. L. Seyler, D. Zhong, E. Schmidgall, M. A. McGuire, D. H. Cobden, W. Yao, D. Xiao, P. Jarillo-Herrero, and X. Xu, Layer-dependent ferromagnetism in a van der Waals crystal down to the monolayer limit, Nature (London) **546**, 270 (2017).

[48] Z. Li, J. Li, K. He, X. Wan, W. Duan, and Y. Xu, Tunable interlayer magnetism and band topology in van der Waals heterostructures of $MnBi_2Te_4$-family materials, Phys. Rev. B **102**, 081107(R) (2020).

[49] S. Mahatara and B. Kiefer, Layer dependent magnetism and topology in monolayer and bilayers ReX_3 (X = Br, I), J. Phys.: Condens. Matter **33**, 455801 (2021).

[50] P.-J. Guo, X.-Q. Lu, W. Ji, K. Liu, and Z.-Y. Lu, Quantum spin Hall effect in monolayer and bilayer $TaIrTe_4$, Phys. Rev. B **102**, 041109(R) (2020).

[51] A. Sufyan, G. Macam, C.-H. Hsu, Z.-Q. Huang, S.-M. Huang, H. Lin, and F.-C. Chuang, Theoretical prediction of topological insulators in two-dimensional ternary transition metal chalcogenides (MM′X4, M = Ta, Nb, or V; M′ = Ir, Rh, or Co; X = Se or Te), Chin. J. Phys. **73**, 95 (2021).

[52] G. Shipunov, B. R. Piening, C. Wuttke, T. A. Romanova, A. V. Sadakov, O. A. Sobolevskiy, E. Yu. Guzovsky, A. S. Usoltsev, V. M. Pudalov, D. V. Efremov, S. Subakti, D. Wolf, A. Lubk, B. Büchner, and S. Aswartham, Layered van der Waals topological metals of $TaTMTe_4$ (TM = Ir, Rh, Ru) family, J. Phys. Chem. Lett. **12**, 6730 (2021).

[53] M. Lv, G. Yu, and W. Chen, 2D $NbIrTe_4$ and $TaRhTe_4$ monolayers: Two fascinating topological insulators as electrocatalysts for oxygen reduction, Inorg. Chem. Front. **9**, 6133 (2022).

[54] D. Kumar, C.-H. Hsu, R. Sharma, T.-R. Chang, P. Yu, J. Wang, G. Eda, G. Liang, and H. Yang, Room-temperature nonlinear Hall effect and wireless radiofrequency rectification in Weyl semimetal $TaIrTe_4$, Nat. Nanotechnol. **16**, 421 (2021).

[55] C. Wang, Y. Zhang, J. Huang, S. Nie, G. Liu, A. Liang, Y. Zhang, B. Shen, J. Liu, C. Hu, Y. Ding, D. Liu, Y. Hu, S. He, L. Zhao, L. Yu, J. Hu, J. Wei, Z. Mao, Y. Shi *et al.*, Observation of Fermi arc and its connection with bulk states in the candidate type-II Weyl semimetal WTe_2, Phys. Rev. B **94**, 241119(R) (2016).

[56] Y. Shi, J. Kahn, B. Niu, Z. Fei, B. Sun, X. Cai, B. A. Francisco, D. Wu, Z.-X. Shen, X. Xu, D. H. Cobden, and Y.-T. Cui, Imaging quantum spin Hall edges in monolayer WTe_2, Sci. Adv. **5**, eaat8799 (2019).

[57] A. Lau, R. Ray, D. Varjas, and A. R. Akhmerov, Influence of lattice termination on the edge states of the quantum spin Hall insulator monolayer $1T'$-WTe_2, Phys. Rev. Mater. **3**, 054206 (2019).

[58] S. Ok, L. Muechler, D. Di Sante, G. Sangiovanni, R. Thomale, and T. Neupert, Custodial glide symmetry of quantum spin Hall edge modes in monolayer WTe_2, Phys. Rev. B **99**, 121105 (2019).

[59] See Supplemental Material at http://link.aps.org/supplemental/10.1103/PhysRevMaterials.8.094201 for further information on (i) crystal structures used, (ii) surface spectral function for different edge terminations in monolayer $TaRhTe_4$, (iii) strain effect of monolayer $TaRhTe_4$, (iv) exfoliation energy and formation energy of monolayer and bilayer $TaRhTe_4$, (v) phonon spectrum for both monolayer and bilayer $TaRhTe_4$, (vi) layer-resolved band weight of bilayer $TaRhTe_4$, (vii) band structure and Wilson loops of AA-stacked bilayer $TaRhTe_4$, and (viii) the DFT bandstructure for bulk $TaRhTe_4$.

[60] M. Hu, G. Ma, C. Y. Wan, and J. Liu, Realistic tight-binding model for monolayer transition metal dichalcogenides of $1T'$ structure, Phys. Rev. B **104**, 035156 (2021).

[61] R. Yu, X. L. Qi, A. Bernevig, Z. Fang, and X. Dai, Equivalent expression of Z_2 topological invariant for band insulators using the non-Abelian Berry connection, Phys. Rev. B **84**, 075119 (2011).

[62] D. Culcer, A. C. Keser, Y. Li, and G. Tkachov, Transport in two-dimensional topological materials: recent developments in experiment and theory, 2D Mater. **7**, 022007 (2020).

[63] A. A. Soluyanov and D. Vanderbilt, Computing topological invariants without inversion symmetry, Phys. Rev. B **83**, 235401 (2011).

[64] S. M. Shinde, K. P. Dhakal, X. Chen, W. S. Yun, J. D. Lee, H. Kim, and J.-H. Ahn, Stacking-controllable interlayer coupling and symmetric configuration of multilayered MoS_2, NPG Asia Mater. **10**, e468 (2018).

[65] F. Wu, T. Lovorn, E. Tutuc, I. Martin, and A. H. MacDonald, Topological insulators in twisted transition metal dichalcogenide homobilayers, Phys. Rev. Lett. **122**, 086402 (2019).

[66] J. H. Jung, C.-H. Park, and J. Ihm, A rigorous method of calculating exfoliation energies from first principles, Nano Lett. **18**, 2759 (2018).

[67] J. Liu, H. Wang, C. Fang, L. Fu, and X. Qian, van der Waals stacking-induced topological phase transition in layered ternary transition metal chalcogenides, Nano Lett. **17**, 467 (2017).

[68] https://www.materialscloud.org/discover/2dtopo/details/RhTaTe4.

[69] K. Koepernik and H. Eschrig, Full-potential nonorthogonal local-orbital minimum-basis band-structure scheme, Phys. Rev. B **59**, 1743 (1999).

[70] https://www.fplo.de.

[71] J. P. Perdew, K. Burke, and M. Ernzerhof, Generalized gradient approximation made simple, Phys. Rev. Lett. **77**, 3865 (1996).

[72] W. Wang, S. Dai, X. Li, J. Yang, D. J. Srolovitz, and Q. Zheng, Measurement of the cleavage energy of graphite, Nat. Commun. **6**, 7853 (2015).

[73] Z. Liu, J. Z. Liu, Y. Cheng, Z. Li, L. Wang, and Q. Zheng, Interlayer binding energy of graphite: A mesoscopic determination from deformation, Phys. Rev. B **85**, 205418 (2012).

[74] G. Kresse and J. Furthmüller, Efficient iterative schemes for *ab initio* total-energy calculations using a plane-wave basis set, Phys. Rev. B **54**, 11169 (1996).

[75] A. Togo, F. Oba, and I. Tanaka, First-principles calculations of the ferroelastic transition between rutile-type and $CaCl_2$-type SiO_2 at high pressures, Phys. Rev. B **78**, 134106 (2008).

[76] P. E. Blöchl, Projector augmented-wave method, Phys. Rev. B **50**, 17953 (1994).